ELSEVIER

CrossMark

BRACHYTHERAPY

Brachytherapy 23 (2024) 73–84

# Heterogeneous physical phantom for I-125 dose measurements and dose-to-medium determination

Paula Cristina Guimarães Antunes[1,2,*], Paulo de Tarso Dalledone Siqueira[1], Julian Marco Barbosa Shorto[1], Hélio Yoriyaz[1]

[1] *Instituto de Pesquisas Energéticas e Nucleares – IPEN-CNEN/SP, Sao Paulo, Brazil*
[2] *Institute of Physics, University of Sao Paulo, Sao Paulo, Brazil*

**ABSTRACT**

**PURPOSE:** In this paper we present a further step in the implementation of a physical phantom designed to generate sets of "true" independent reference data as requested by TG-186, intending to address and mitigate the scarcity of experimental studies on brachytherapy (BT) validation in heterogeneous media. To achieve this, we incorporated well-known heterogeneous materials into the phantom in order to perform measurements of $^{125}$I dose distribution. The work aims to experimentally validate Monte Carlo (MC) calculations based on MBDCA and determine the conversion factors from LiF response to absorbed dose in different media, using cavity theory.

**METHODS AND MATERIALS:** The physical phantom was adjusted to incorporate tissue equivalent materials, such as: adipose tissue, bone, breast and lung with varying thickness. MC calculations were performed using MCNP6.2 code to calculate the absorbed dose in the LiF and the dose conversion factors (DCF).

**RESULTS:** The proposed heterogeneous phantom associated with the experimental procedure carried out in this work yielded accurate dose data that enabled the conversion of the LiF responses into absorbed dose to medium. The results showed a maximum uncertainty of 6.92 % ($k=1$), which may be considered excellent for dosimetry with low-energy BT sources.

**CONCLUSIONS:** The presented heterogeneous phantom achieves the required precision in dose evaluations due to its easy reproducibility in the experimental setup. The obtained results support the dose conversion methodology for all evaluated media. The experimental validation of the DCF in different media holds great significance for clinical procedures, as it can be applied to other tissues, including water, which remains a widely utilized reference medium in clinical practice.


*Keywords:* Brachytherapy; Heterogeneous phantom; Experimental dosimetry; $^{125}$I seed; LiF, MBDCA; Dose-to-medium; Monte Carlo; Dose conversion factor

## Introduction

Radioactive iodine-125 ($^{125}$I) sealed sources have been highly successful in treating various types of cancer, such as head and neck, inoperable brain tumors, oral/maxillofacial, pulmonary, hepatic, pancreatic, and, most commonly, prostate cancers (1–7). The increasing number of applications can be attributed to significant advancements in brachytherapy (BT) techniques over the past few decades, among which the following stand out: evolution of seed implantation procedures from ultrasound guidance to computed tomography guidance; real-time dosimetry optimizations; improvements in treatment planning using 3D-individual printed models and the integration of artificial intelligence, seeking to enhance reproducibility and prevent seed migration (1,8). Furthermore, important enhancements to the planning system have contributed to the notable improvement in the accuracy of $^{125}$I BT (9).

These advancements have enabled the delivery of higher and most conformal doses in the target lesion while minimizing exposure to surrounding normal tissue, reducing side effects and toxicity due to the sharp dose drop-off outside the target lesion (1). However, this evolution brings

Received 17 April 2023; received in revised form 30 July 2023; accepted 30 August 2023

Disclosures: The authors declare that they do not have any conflict of interest.

* Corresponding author. Instituto de Pesquisas Energéticas e Nucleares – IPEN-CNEN/SP, Av. Prof. Lineu Prestes, 2242 Sao Paulo, 05508000, Brazil.

*E-mail address:* pacrisguian@gmail.com (P.C.G. Antunes).

1538-4721/$ - see front matter 
https://doi.org/10.1016/j.brachy.2023.08.007

with it questions related to the precision in dose estimation, particularly with regard to the resulting planned dose proposed by treatment planning systems (TPS) and the experimental validation of these dose distributions (10).

Traditionally and worldwide, BT dosimetry has been based on the formalism recommended by the American Association of Physicists in Medicine (AAPM) - Task Group report No. 43 (TG-43) (11–14). This formalism describes dose deposition around a single source positioned in an infinite water phantom. Consequently, the absorbed dose has been computed and reported as dose to water in water ($D_{w,w}$). This approach has formed the basis for most clinical experiences, with Monte Carlo (MC) and experimental consensus datasets being widely discussed in the literature (14,15). However, it may not accurately represent certain clinical situations, mainly due to neglecting human tissue densities, material compositions, finite dimensions of the patient anatomy, and dose perturbations from applicators (10,15–18).

To address the need for more realistic dose calculations, the AAPM published TG-186 in 2012, which introduced the model-based dose calculation algorithm (MBDCA) for BT (10). TPS based on this algorithm can consider the complexities mentioned above by calculating the dose to medium in medium ($D_{m,m}$). This approach takes into account energy deposition in handling medium compositions/density and other treatments complexities and offers an excellent dose-response relationship.

Despite the clear benefits of $D_{m,m}$, its proper implementation in BT clinical practice requires additional efforts, especially considering the strong dependency on medium composition. Uncertainties in medium composition will affect absorbed dose estimates, playing a more significant impact for low-dose-rate (LDR) BT applications. Scenarios involving low-energy photons ($< 100$ keV) and high-Z elements in the medium, such as bone, can have an even greater effect (10,15,19-22).

The dose conversion factors (DCF) between $D_{w,w}$ and $D_{m,m}$ are based on cavity theory and have been extensively studied to transition from the TG-43 to TG-186 dose calculation approach. These factors aim to associate all previously acquired knowledge based on the initial BT protocols, with dose calculations performed in water, with the dose calculated in the medium using modern MBDCA (15–17,23–25).

According to TG-186, one of the main issues to move towards MBDCA, is the evolution of experimental procedures in order to consider the heterogeneity of the medium and enable the experimental validation of absorbed dose obtained through MC calculations. However, there is a lack of information on experimental BT, with limited studies based on TG-186 (26,27). This scarcity can be attributed to the challenges associated with accurately measuring experimental data, especially for low-energy BT (28).

One of the main recommendations of TG-186 is the design and implementation of relevant physical phantom with well-known materials, using dosimeters such as TLDs, radiochromic films, and GEL dosimeters, to evaluate dose distributions experimentally and compare them to the virtual representation within a MBDCA TPS. These efforts aim to generate sets of "true" independent reference data that allow the validation of the TPS.

With this in mind, we previously developed a versatile phantom that aligns the recommendation presented by TG-186 (28). This phantom ensures precise experimental dose evaluations through its simple, cost-effective design, and easy reproducibility of experimental setups. Initially constructed with PMMA, the phantom allowed the generation of accurate experimental BT dose data in PMMA medium. Within this context, the current work represents a further evolution of the previous phantom, with the insertion of known heterogeneous materials, addressing three main objectives: *(1)* to perform measurements of $^{125}$I experimental dose distribution in some tissue equivalent materials (adipose tissue, bone, breast and exhaled lung) using LiF dosimeters; *(2)* to validate the MC calculations with MBDCA using the experimental LiF dose data, and *(3)* to convert the experimental LiF dose ($D_{LiF,m}$) into absorbed dose in different media in media ($D_{m,m}$), using cavity theory and MC calculations.

## Methods and materials

### *Proposed phantom*

Figure 1 shows the physical phantom geometry used in this work. It represents an evolution of the previously introduced phantom (28) and has been adapted to accommodate some tissue equivalent materials (TEM) in its intermediate section.

This phantom consists of a set of three square ($100 \times 100$ mm$^2$) PMMA sections, which are assembled one onto another. The first section is a 10.0 mm thick slab with a central cavity on its top surface to hold the LiF dosimeter. The second section consists of one or more PMMA slabs that have been machined to allow the insertion of TEM, resulting in a section with variable thickness ($z$). Lastly, the third section is a 10.0 mm thick superior slab with a central cavity on its bottom surface designed to hold the $^{125}$I seed.

Ten phantoms were used simultaneously in the experimental procedure carried on during this work. These phantoms differ from each other in the second section, where both slab thickness and material medium vary. Four different TEM of CIRS (Tissue Simulation & Phantom Technology) (29) were introduced: adipose tissue, bone, breast 50/50, and exhaled lung. The main atomic compositions and mass density values of the phantom materials are given in Table 1.

The TEM inserted into the phantoms consists of 30.0 mm diameter cylinders machined in different thicknesses ($z$), to fit into the slabs which constitute the interme-

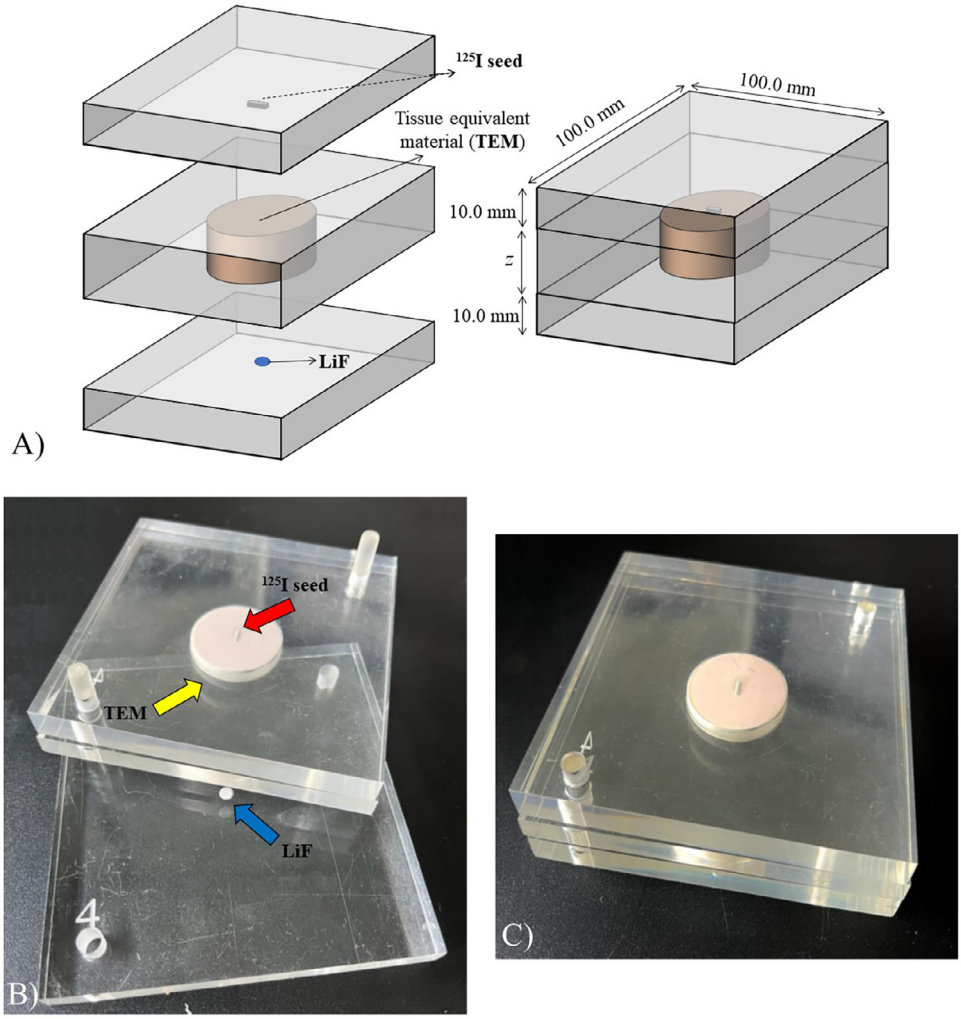


Fig. 1. (a) Schematic illustration of the heterogeneous phantom used in this work. (b) Picture of the phantom, with red and blue arrows showing PMMA slabs with $^{125}$I seed and LiF, respectively. Yellow arrow shows the cylindrical tissue equivalent material (TEM) inserted into the second section. (c) Phantom arranged in its irradiation configuration. (For interpretation of the references to color in this figure legend, the reader is referred to the web version of this article.)

Table 1
Phantom materials elemental compositions (mass fractions), Effective Atomic numbers ($Z_{eff}$), and densities.

| Material | Adipose tissue | Bone | Breast | Lung | PMMA |
|---|---|---|---|---|---|
| H | 0.100 | 0.045 | 0.096 | 0.089 | 0.080 |
| C | 0.713 | 0.354 | 0.704 | 0.660 | 0.600 |
| N | 0.018 | 0.012 | 0.019 | 0.024 | - |
| O | 0.164 | 0.294 | 0.170 | 0.204 | 0.320 |
| P | - | 0.092 | - | - | - |
| Cl | 0.002 | 0.001 | 0.002 | 0.006 | - |
| Ca | 0.003 | 0.199 | 0.009 | 0.017 | - |
| Others | - | 0.003 | - | - | - |
| Density (g/cm³) | 0.960 | 1.660 | 0.991 | 0.510 | 1.190 |
| $Z_{eff}$ | 6.380 | 12.670 | 6.830 | 7.410 | 6.530 |

diate/second section of the phantom, setting the source-detector distance and measuring the percentage depth dose (PDD) for different materials. Some distances were achieved by assembling two or more slabs of thinner thicknesses. The specific thicknesses ($z$) employed in the phantom configurations for each TEM are presented in Table 2. Thicknesses and uncertainties were evaluated by the mean values and their mean standard deviation ($1\ \sigma$) driven from a series of experimental measurements performed using a micrometer screw.

These materials exhibit varying thicknesses due to imperfections and uncertainties introduced during the machining process. Some TEM, such as lung, are inherently more porous, which leads to the loss of material in the machining process resulting in a reduced number of TEM thicknesses.

Model Amersham 6711 (OncoSeed - GE Healthcare, IL. Marketed by Oncura, Inc) $^{125}$I brachytherapy seeds, with initial activities of 1 mCi, were used. Four batches of 10 seeds were used throughout the experiments.

Table 2
TEM thicknesses ($z$) attained for the second section with their respective uncertainties.

| Tissue equivalent materials | | | | |
|---|---|---|---|---|
| | Adipose tissue | Bone | Breast | Lung |
| ($z$) (mm) | 1.844±0.011 | 1.950±0.015 | 1.740±0.012 | 1.900±0.027 |
| | 2.340±0.032 | 2.039±0.005 | 2.400±0.016 | 2.820±0.014 |
| | 3.254±0.007 | 2.880±0.009 | 3.999±0.015 | 4.820±0.008 |
| | 4.803±0.005 | 2.969±0.018 | 4.251±0.008 | 7.400±0.001 |
| | 7.781±0.008 | 4.600±0.019 | 6.812±0.008 | 7.801±0.014 |
| | 8.235±0.011 | 4.998±0.004 | 8.938±0.016 | - |
| | 10.398±0.016 | 6.903±0.016 | 10.028±0.016 | - |
| | 12.242±0.019 | 7.680±0.018 | 11.768±0.020 | - |

*LiF methodology*

LiF:Mg,Ti dosimeters (Thermofisher,Waltham, Massachusetts) known as TLD-700 in a disk format of 0.254 mm thick and 3.6 mm in diameter were used in this work (30,31). The LiF dosimetry procedures were consistent with those described in the previous work (28). To prepare the dosimeters for each irradiation, an annealing procedure was conducted one day in advance, following the method proposed by Davis et al. (32). After each irradiation, LiF readings were taken one day later. The total area under the thermoluminescent glow curve was used as the LiF response intensity ($I_{LiF}$), in $\mu C$ units.

Before the experiments, a total of 36 LiF were selected, using a reproducibility (precision $<$ 3.0 %) criteria. The calibration of absorbed dose sensitivity was performed using a 6 MV X-ray beam produced by a Linac, resulting in an absorbed dose calibration coefficient of $S_D(6MV)$ =32.74 ± 1.25 $\mu$C/Gy (28).

The experimental methodology consisted of irradiating the dosimeters within 10 phantoms, similar to that shown in Fig. 1, with different settings in the second section. Phantom arrangements varied according to the heterogeneous medium and thickness ($z$) introduced between the LiF dosimeters and the $^{125}$I seed. In all measurements, the irradiation time followed the same procedure used in the previous work (28), adopting the same irradiation time to attain 1.5 mGy calculated air kerma at a 10 cm distance from the seed, in a free vacuum configuration. This particular value was chosen to ensure the feasibility of the irradiation time span throughout the entire lifetime of the seeds.

LiF corrected response for a thickness (z), $R_{LiF(z)}$, in $\mu C$ units, was obtained by the LiF response intensity ($I_{LiF}$) discounting the average of LiF unexposed responses ($\bar{I}_{Background}$), that is, ($I_{LiF(z)} - \bar{I}_{Background}$). The dosimeters were randomly irradiated several times in the same setting, that is, different dosimeters were used to obtain the TLD responses and uncertainties for each thickness ($z$) and TEM, resulting in mean values $\overline{R}_{LiF,m(z)}$ corrected response with radiation transport performed in different media $m$. On average, 12 irradiations were performed for each experimental arrangement.

*Dose to medium from experimental values*

Four different media were used: adipose tissue, bone, breast 50/50 and exhaled lung. The dose to medium determined from experimental data ($\overline{R}_{LiF,m(z)}$), can be estimated by Eq. (1), adopting the methodology previously presented in Antunes et al. (28) and in TG-43 (14).

$$D_{m,m(z)}\left(^{125}I\right) = \overline{R}_{LiF,m(z)}\left(^{125}I\right).N_D(6MV).f^{rel}.k_{bq}^{rel} \quad (1)$$

where $D_{m,m(z)}$ is the absorbed dose to medium $m$ with transport performed in medium $m$, $N_D(6MV) = 1/S_D(6MV)$ is the absorbed dose calibration coefficient at the calibration radiation quality, $f^{rel}$ is the LiF relative absorbed dose energy dependence and $k_{bq}^{rel}$ is the LiF relative intrinsic energy dependence, both with respect to the 6 MV calibration beam. $k^{rel}$ value used is 0.931 ± 0.013 (33), following the recommendation of the TG-43 (14). $f^{rel}$ was calculated by MC from Eq. (2), to take into account the different absorbed dose energy dependence of the LiF in the $^{125}$I beam quality and 6 MV X-ray.

$$f^{rel} = \frac{f\left(^{125}I\right)}{f(6MV)} = \frac{[D_{m,m}/D_{LiF,m}]_{^{125}I}}{[D_{PMMA,PMMA}/D_{LiF,PMMA}]_{6MV}} \quad (2)$$

where $D_{LiF,m}$ is the absorbed dose in the LiF with transport performed in medium $m$, considering the composition and dimension of the studied dosimeter, and $D_{LiF,PMMA}$ is the absorbed dose in the LiF with transport performed in PMMA.

The denominator $[D_{PMMA,PMMA}/D_{LiF,PMMA}]_{6MV}$ in the above equation was estimated in the previous work through MC calculations, as equal to 1.096±0.018 (28). The numerator was obtained in this work from MC calculations that accounted for the geometry and physical properties of both LiF and phantom in the experimental irradiation configurations performed for the different studied media.

Under the large cavity theory assumption (16,17), the relation between dose to medium and dose to LiF can therefore be written as:

$$\frac{D_{m,m}}{D_{LiF,m}} = \frac{(\overline{\mu}_{en}/\rho)_{m,m}.\Psi_{m,m}}{(\overline{\mu}_{en}/\rho)_{LiF,m}.\Psi_{LiF,m}} \quad (3)$$

where $\Psi_{m,m}$ and $\Psi_{LiF,m}$ are the total photon energy-fluences in medium and in LiF, respectively, and $(\overline{\mu}_{en}/\rho)_{m,m}$ and $(\overline{\mu}_{en}/\rho)_{LiF,m}$ are the mass energy-absorption coefficients of TEM and LiF, averaged over the local photon energy-fluence.

Eq. (3) can be rewritten in its ratio form as:

$$\frac{D_{m,m}}{D_{LiF,m}} = (\overline{\mu}_{en}/\rho)^{m,m}_{LiF,m}.\Psi^{m,m}_{LiF,m} \quad (4)$$

where $\Psi^{m,m}_{LiF,m}$ is the energy-fluence ratio, and $(\overline{\mu}_{en}/\rho)^{m,m}_{LiF,m}$ is the ratio of energy-fluence weighted average mass energy-absorption coefficients, both with respect to TEM and LiF. In order to simplify the ratio from notation, the specification of the medium ($m$) in which the radiation is transported was suppressed. In this way, $(\overline{\mu}_{en}/\rho)^{m,m}_{LiF,m}$ in the Eq. (4) will be renamed to $(\overline{\mu}_{en}/\rho)^{m}_{LiF}$, for example.

In this sense, we can rewrite the Eq. (2) as:

$$f^{rel} = \frac{f(^{125}I)}{f(6MV)} = \frac{\left[(\overline{\mu}_{en}/\rho)^{m}_{LiF}.\Psi^{m}_{LiF}\right]_{^{125}I}}{\left[D_{PMMA,PMMA}/D_{LiF,PMMA}\right]_{6MV}} \quad (5)$$

with $\Psi^{m}_{LiF}$ and $(\overline{\mu}_{en}/\rho)^{m}_{LiF}$ factors MC-scored as described in the previous work (28).

All dose calculations have been done using the Monte Carlo N-Particle – MCNP code version 6.2 (34), according to the methodology described in Antunes et al. (28). The number of primary photons was set to $4 \times 10^9$ for all simulations, providing uncertainties below 0.4 % (Type A $\pm$ 1$\sigma$). Each simulation run was performed using a 90 core Intel Xeon processor, taking approximately 190 min of computational time.

Adopting the proposed terminology, superscript indices will be employed to designate the procedure used to evaluate the dose: *conv* and *MC* to designate, respectively, the absorbed dose obtained from the conversion through cavity theory, and the absorbed dose calculated by MC calculation. Consequently, $D_{m.m}$ of the Eq. (1) will be renamed to $D^{conv.}_{m,m}$.

### *Data analysis*

Data analysis was carried out through the residual defined according to Eq. (6) for Fig. 2.

$$residual_{(z)} = \frac{\left(\overline{R}_{LiF,m(z)}\right)_{Norm.} - \left(D^{MC}_{LiF,m(z)}\right)_{Norm.}}{\left(\sigma_{\overline{R}_{LiF,m(z)}}\right)_{Norm.}} \quad (6)$$

where $(\overline{R}_{LiF,m(z)})_{Norm.}$ is the average of the normalized experimental values at each thickness $z$ with its respective propagated uncertainty $(\sigma_{\overline{R}_{LiF,m(z)}})_{Norm.}$ and, $(D^{MC}_{LiF,m(z)})_{Norm.}$ represents the normalized calculated values by MC. The residuals are dimensionless.

### *Uncertainty budget*

Table 3 presents the uncertainties associated with both experimental and calculated values leading to a maximum final total uncertainty of 6.92 %. The uncertainty associated with MC calculations encompasses the statistical uncertainties (Type A) which is inherent to MC tally procedure, as well as Type B uncertainties resulting from the seed geometry and energy spectrum modelling. These uncertainty components align with the methodology outlined by Kennedy et al. (35).

The reported uncertainty values are presented using a coverage factor k=1 (i.e., 1 $\sigma$). The type A uncertainty assigned to repetitive LiF measurements was estimated from the standard deviation of the mean value. LiF responses $\overline{R}_{LiF,m(z)}$ and uncertainties were measured for each one of the thicknesses ($z$) and media presented in Table 2. Data were collected at an amount that suffices both the best estimate values, given by the average responses, and uncertainty estimates, given by the mean standard deviations.

BT dosimetry measurements involve numerous parameters that can contribute to the overall uncertainties (36). In the previous work (28), a comprehensive discussion was presented regarding the uncertainty factors associated with the phantom and the experimental methodology, through a phantom sensitivity analysis. In this analysis we evaluated the combined impact of various factors, including material thickness and density, phantom structures alignment, LiF holder oversize, internal source displacement, LiF sensitivity, and LiF reader efficiency. The purpose of this analysis was to provide a general view of the potential uncertainties inherent in the proposed phantom.

## Results

### *Phantom measurements*

Figure 2 shows the experimental and simulated PDD for the four evaluated media as a function of thickness ($z$), $(\overline{R}_{LiF,m(z)})_{Norm.}$ and $(D^{MC}_{LiF,m(z)})_{Norm.}$, respectively. Additionally, to assist in the analysis of the results, the graph below displays the residuals between the two curves, calculated using Eq. (6).

The experimental values, $(\overline{R}_{LiF,m(z)})_{Norm.}$, corresponds to the average LiF response value obtained after a set of irradiations performed for each thickness and medium. The uncertainties are determined by the mean standard deviation. In general, to achieve comparable uncertainties throughout the entire range of the PDD, a larger number of measurements were performed for the smallest thicknesses in all media compared to the thickest ones, as they are in a region closer to the seed and with a higher dose gradient. $(D^{MC}_{LiF,m(z)})_{Norm.}$ and $(\overline{R}_{LiF,m(z)})_{Norm.}$ values exhibit consistent behaviour across all evaluated TEM and thicknesses, with differences consistently within the range of experimental uncertainties. The thicknesses used to

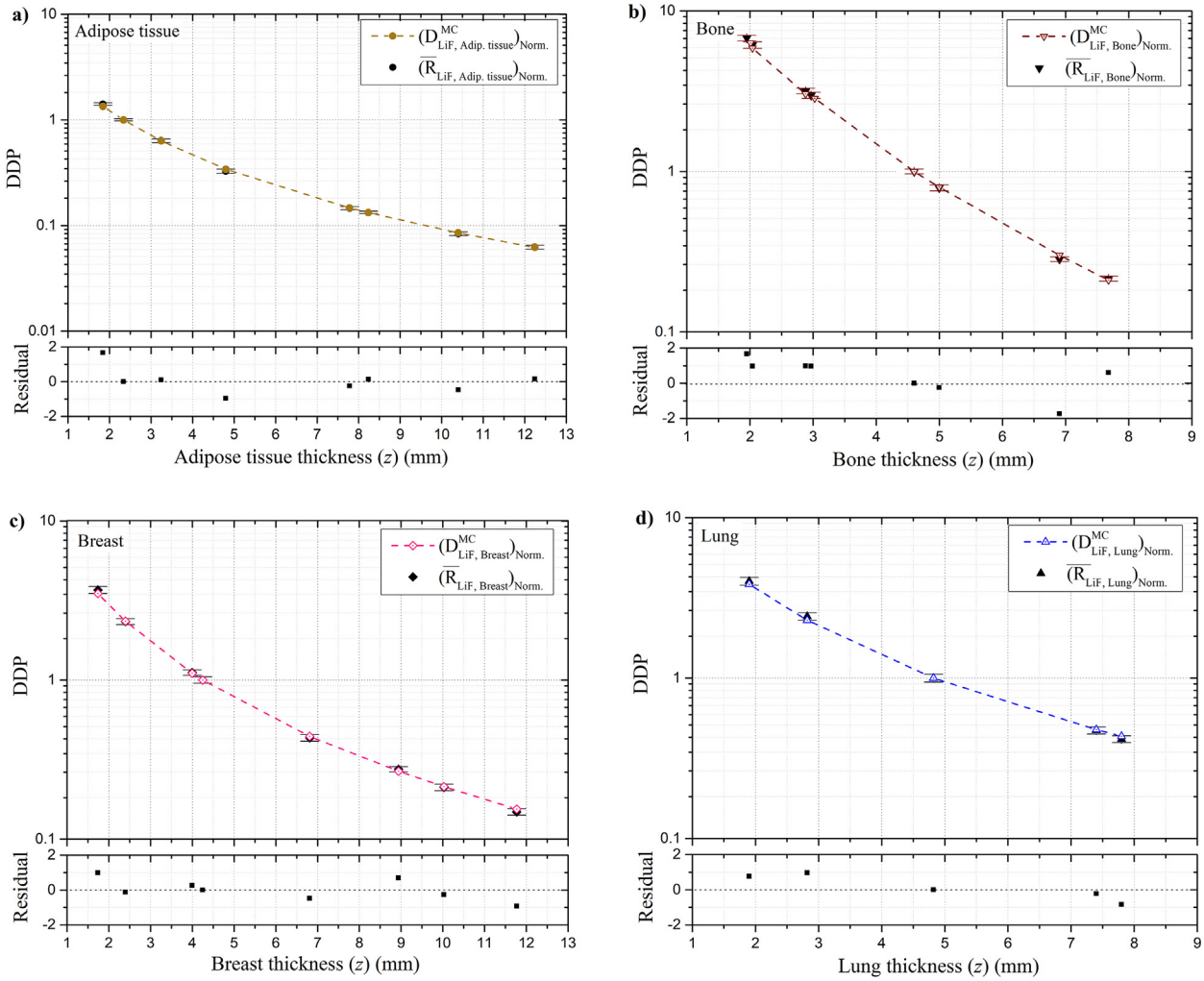


Fig. 2. Top – Percentage Depth Dose – PDD, for different media (a - Adipose tissue; b - Bone; c - Breast and d - Lung) to perform the radiation transport: Simulated $(D^{MC}_{LiF,m})_{Norm.}$, open coloured signal and experimental $(\overline{R}_{LiF,m})_{Norm.}$, black signal. Dotted lines are only guidelines. Bottom – Residuals, taking simulated values as reference. (For interpretation of the references to color in this figure legend, the reader is referred to the web version of this article.)

Table 3
Analysis of the associated uncertainties.

| Source of uncertainty | Dosimetric uncertainty (%) | |
|---|---|---|
| | Type A | Type B |
| Average of repetitive measurements | 5.25[a] | |
| LiF dose calibration | | 3.82 |
| Relative absorbed dose energy dependence, $f^{rel}$ | | 1.68 |
| Relative absorbed dose energy dependence, $k^{rel}$ | | 1.40 |
| Monte Carlo results | 0.90 | 0.33 |
| Quadratic sum | 5.33 | 4.41 |
| Combined total uncertainty ($k=1$) | 6.92 | |

Random or statistical effects are described as Type A uncertainties and Type B uncertainties describe systematic effects.

[a] for the maximum value found for the thickness of $z=6.903 \pm 0.016$ mm of bone.

normalize the experimental and simulated data differ for each evaluated TEM, due to the availability of different thicknesses for each medium. In general, the thicknesses that yielded a lower experimental uncertainty in LiF response were selected to normalize the corresponding PDD.

### *Relative absorbed-dose energy dependence $f^{rel}$*

$f(^{125}I)$ was estimated for each evaluated TEM from the $\Psi^m_{LiF}$ and $(\overline{\mu}_{en}/\rho)^m_{LiF}$ MC-scored quantities. The values of $\Psi^m_{LiF}$ were evaluated for each thickness ($z$) based

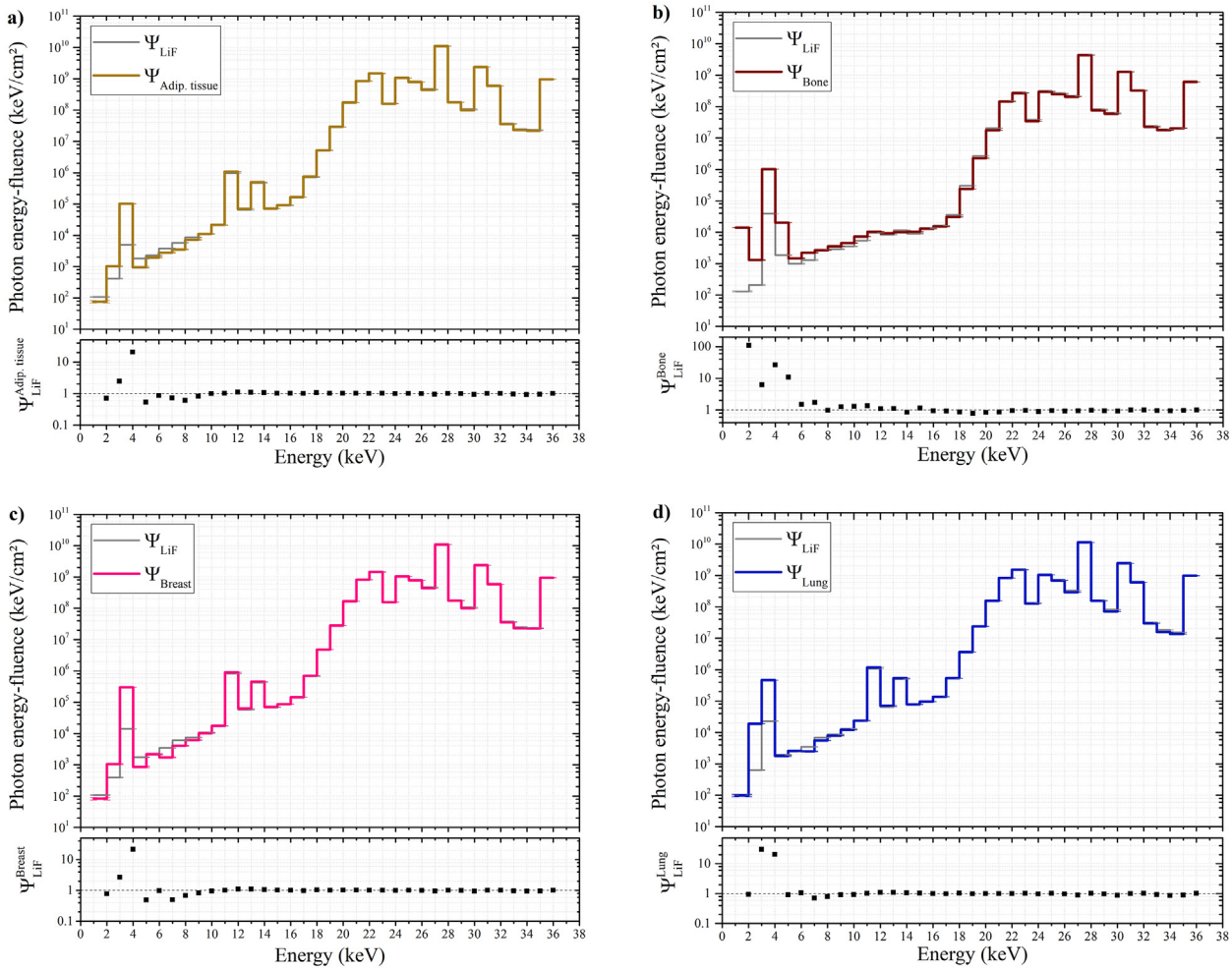


Fig. 3. Top: calculated photon energy-fluence spectra in the detector cavity either filled with LiF (gray line) or filled with tissue equivalent material (coloured line) for the thickness of TEM of $z = 4.00$ mm. (a) Adipose tissue (dark yellow line); (b) Bone (wine line); (c) Breast (pink line); (d) Lung (blue line). Bottom: the corresponding energy-fluence ratio value $\Psi^m_{LiF}$ . (For interpretation of the references to color in this figure legend, the reader is referred to the web version of this article.)

on the photon energy-fluence in the cavity (LiF or TEM). Figure 3 shows the $\Psi_{LiF}$ and $\Psi_m$ as a function of energy for each evaluated propagation medium. In all cases a TEM thickness of $z = 4.00$ mm was used.

The photon energy-fluence spectra calculated for LiF and media/TEM exhibit considerable overlap, yielding similar results with differences within the statistical uncertainties, except for energies below 12 keV. The integral photon energy-fluence was calculated for both LiF and TEM across all thicknesses used in the phantoms throughout this work. The average energy-fluence ratio value is presented in Table 4.

The parameter $(\overline{\mu}_{en}/\rho)^m_{LiF}$ was evaluated, for each $(z)$, by taking the ratio of mass energy-absorption coefficients of the TEM and LiF, averaged over the local photon energy-fluence. The calculated values remained constant for the different thicknesses $(z)$ of each TEM, resulting in average values that are presented in Table 4, with their respective propagated uncertainties.

Table 4
Calculated energy-fluence correction factors ($\Psi^m_{LiF}$) and energy-fluence weighted mass energy-absorption coefficient $(\overline{\mu}_{en}/\rho)^m_{LiF}$.

| Medium | $\Psi^m_{LiF}$ | $(\overline{\mu}_{en}/\rho)^m_{LiF}$ |
|---|---|---|
| Adipose tissue | (1.0049±0.0018) | (0.4879±0.0005) |
| Bone | (0.9732±0.0049) | (5.3019±0.0131) |
| Breast | (1.0055±0.0011) | (0.6119±0.0002) |
| Lung | (1.0042±0.0011) | (0.8569±0.0003) |

To validate the obtained $\Psi^m_{LiF}$ and $(\overline{\mu}_{en}/\rho)^m_{LiF}$ parameters, $D^{MC}_{LiF,m}$ and $D^{MC}_{m,m}$ were calculated for different TEM thicknesses $(z)$ from 1.0 mm to 14.0 mm range, with increments of 1.0 mm. These estimates were multiplied by the square of the material thickness $(z^2)$, so to have the square of distance geometric dependence factored out from the results, before been shown in Fig. 4. All dose values were estimated using tally *F8, retrieving estimates with Type A uncertainties below 0.2%.

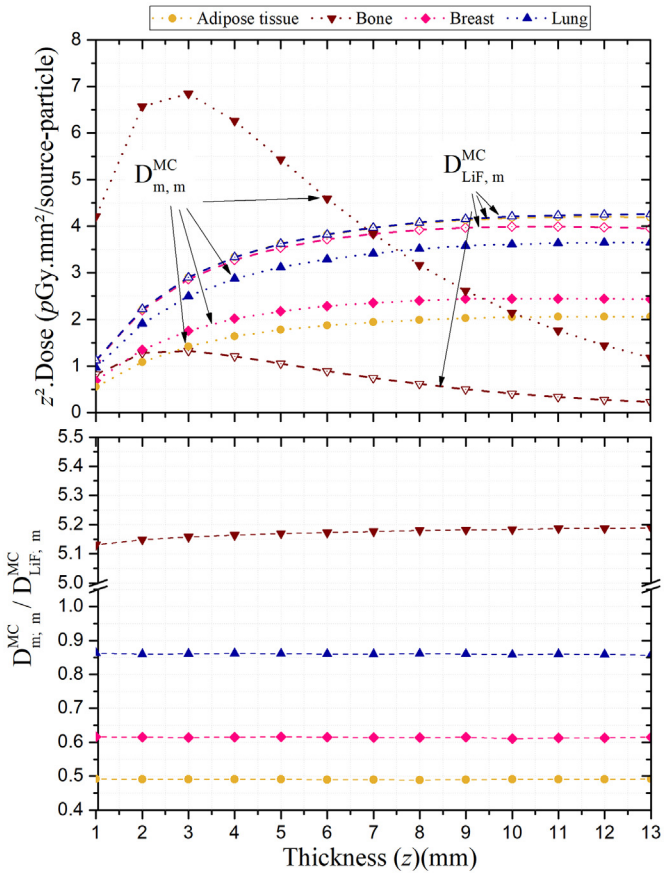


Fig. 4. Top: $D^{MC}_{LiF,m}(z)$ (empty symbols) and $D^{MC}_{m,m}(z)$(filled symbols) times thickness squared value ($z^2$) for different media thicknesses ($z$); Bottom: the corresponding calculated dose ratios, $D^{MC}_{m,m}/D^{MC}_{LiF,m}$. Adipose tissue (dark yellow circles); Bone (wine inverted triangles); Breast (pink diamonds) and Lung (blue triangles). (For interpretation of the references to color in this figure legend, the reader is referred to the web version of this article.)

Table 5
Data for MC calculated ($D^{MC}_{m,m}/D^{MC}_{LiF,m}$) ratio and the ($(\overline{\mu}_{en}/\rho)^{m}_{LiF}.\Psi^{m}_{LiF}$) parameters for different TEM studied.

| Medium | $D^{MC}_{m,m}/D^{MC}_{LiF,m}$ | $(\overline{\mu}_{en}/\rho)^{m}_{LiF}.\Psi^{m}_{LiF}$ |
|---|---|---|
| Adipose tissue | (0.4902±0.0013) | (0.4903±0.0010) |
| Bone | (5.1726±0.0187) | (5.1598±0.0288) |
| Breast | (0.6139±0.0015) | (0.6153±0.0007) |
| Exhaled lung | (0.8601±0.0016) | (0.8604±0.0010) |

In addition to dose profiles, Fig. 4 shows the $D^{MC}_{m,m}/D^{MC}_{LiF,m}$ ratios, which exhibit a constant behaviour as a function of thickness for all TEM, resulting in average values presented in the Table 5.

As already observed in the previous work (28) where PMMA was used as the medium for radiation transport and dose calculation, the excellent agreement between $D^{MC}_{m,m}/D^{MC}_{LiF,m}$ and $(\overline{\mu}_{en}/\rho)^{m}_{LiF}.\Psi^{m}_{LiF}$ values confirms the suitability of the product of $\Psi^{m}_{LiF}$ and $(\overline{\mu}_{en}/\rho)^{m}_{LiF}$ calculated parameters as a reliable dose conversion factor (DCF). This DCF enables the conversion of the LiF experimental dose evaluations into the medium dose estimate: $D^{\exp}_{LiF,m} \rightarrow D^{conv.}_{m,m}$.

### $D^{conv}_{m,m}$ *versus* $D^{MC}_{m,m}$

Following the methodology presented in the previous work (28), the $D^{conv}_{m,m}$ values estimated from experimental data can be used to validate the $D^{MC}_{m,m}$ MC calculations, so that an ideal conversion factor should yield a ratio of $D^{conv}_{m,m}/D^{MC}_{m,m} = 1$. Figure 5 shows this ratio for all thickness values ($z$) of each TEM evaluated within the phantom.

The uncertainties on the ratio values presented in Fig. 5 takes into account the propagation of all uncertainties associated with the LiF measurements and the MC uncertainties associated with both terms of the ratio.

## Discussion

The need to design and implement relevant physical phantom geometries with known materials to generate reference data is well-known in the literature, especially in BT (10). Within this framework, in the previous work (28) we presented a versatile physical phantom design and construction for $^{125}$I dose measurements. This design enables the acquisition of data with the required precision in dose evaluations, due to its easy reproducibility of experimental

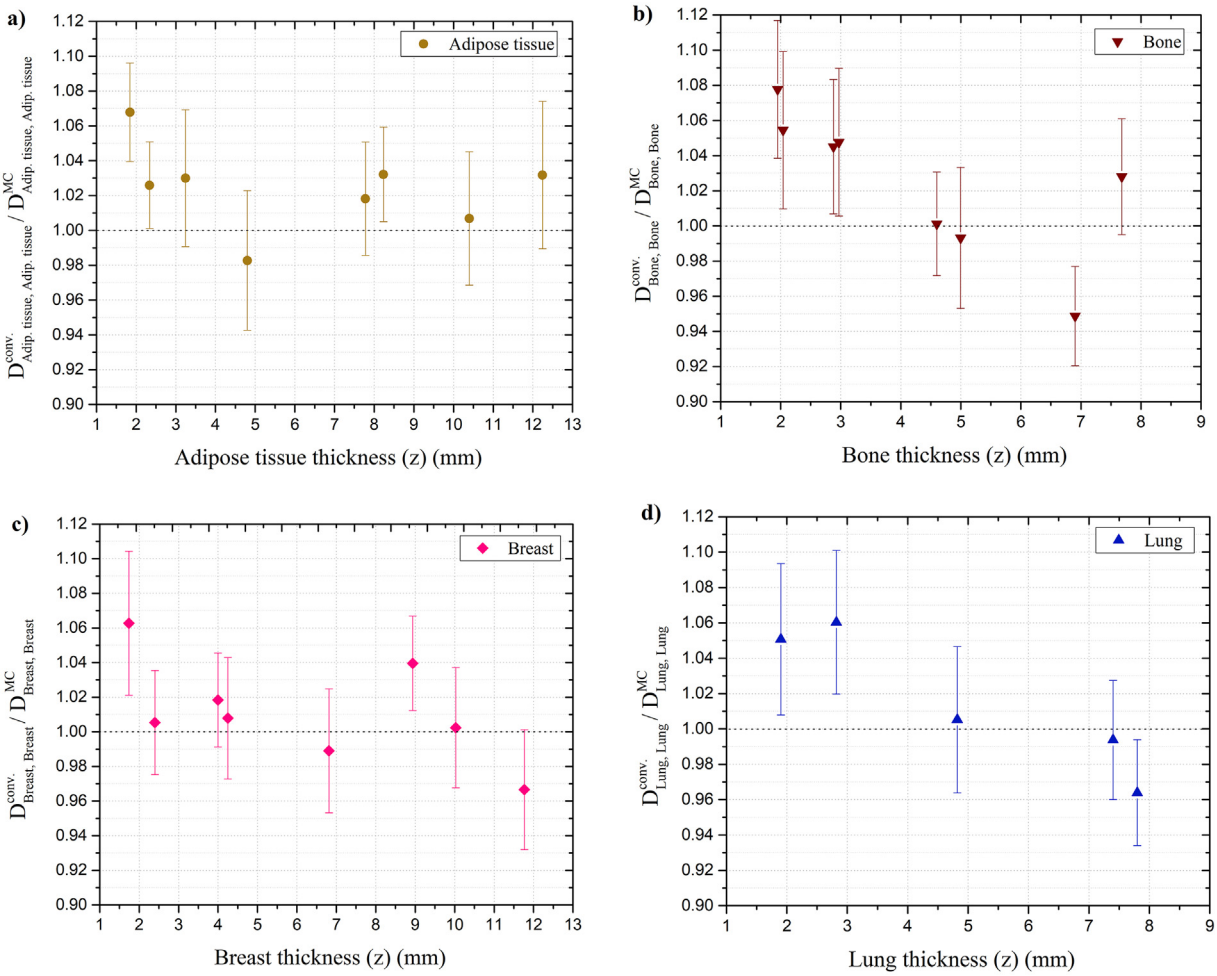


Fig. 5. Ratio between the converted and calculated absorbed doses to medium. (a) adipose tissue; (b) bone; (c) breast; (d) lung. (For interpretation of the references to color in this figure legend, the reader is referred to the web version of this article.)

setup. In the current work, we present the further step on its implementation by incorporating different known heterogeneous materials in the phantom. This modification permits the interposition of different materials between the $^{125}$I source and the LiF detector. Experimental PDD was driven by measurements with various material thicknesses.

Four different tissue equivalent materials were used with this phantom: adipose tissue, bone, breast and lung, with variable thicknesses, seeking to experimentally evaluate the depth dose distributions produced by a $^{125}$I source in different media. These materials were chosen due to their relevance in $^{125}$I BT besides covering a wide range of densities, 0.510-1.660 g.cm$^{-3}$, and $Z_{eff}$, 6.380–12.670, as can be seen in Table 1.

The results presented in Fig. 2 indicate an excellent agreement between LiF experimental data and MCNP calculated data. The magnitude of differences is within propagated experimental uncertainties. Each experimental data in this figure corresponds to the mean value of 12 measurements, on average. In cases where larger uncertainty distributions were observed, a greater number of experimental measurements were conducted to minimize the uncertainty in the mean deviation.

The accurate and laborious experimental data turned the MC calculation validation possible. Experimental data was acquired and calculations were performed for four different media, asserting the validity of the dose to medium conversion methodology presented in the previous work (28). This conversion is carried out from $\Psi^m_{LiF}$ and $(\overline{\mu}_{en}/\rho)^m_{LiF}$ MC-scored quantities: the total photon energy-fluences and the energy-fluence weighted average mass energy-absorption coefficients, respectively, calculated for both TEM ($m$) and detector (LiF).

Figure 3 shows the calculated photon fluences in LiF ($\Psi_{LiF}$) and in each of the four different TEM ($\Psi_m$), for 4.00 mm thickness, as a function of energy. Photon fluences are similar over the energy range except for energies below 12 keV. This difference is primarily due to the prominent influence of the photoelectric effect in the low-energy photon range. This effect is particularly pronounced for high-Z media, as exemplified by the larger differences observed in bone (Fig. 3b). Nevertheless, it is important

to highlight that the conversion methodology relies on the average values of $\Psi^m_{LiF}$, which approach one unit, as can be seen in Table 4.

It is observed that $\Psi^m_{LiF} \approx 1.00$ for low density medium and $Z_{eff}$, such as adipose tissue, breast and exhaled lung. For high density and high $Z_{eff}$ media, such as bone, $\Psi^m_{LiF}$ value diverges from unity stressing the importance of addressing a proper value to get a more exact estimation of the conversion factor. The $\Psi^m_{LiF}$ obtained in this work shows a 3.0 % improvement in the conversion factor exactitude.

Gimenez et al. (15) highlights the importance of the energy-fluence correction factors for different tissues when irradiated with $^{125}$I and $^{103}$Pd seeds, obtaining expressive factors of the energy-fluence ratio, closer to 1.7, for the conversion dose to bone (cortical ICRP) (37) into dose to water. The values calculated in this work (Table 4) are lower than those estimated by Gimenez et al. (15), since the conversion here is between dose to LiF to dose to bone. Although being less significant, these values estimated in our work still demonstrate the importance of $\Psi^m_{LiF}$ for all media, particularly when dealing with the combination of low-energy photons (< 100 keV) and high-Z media. This combination turns the photoelectric effect into the predominant interaction, leading to a higher absorption of low-energy photons and therefore hardening the photon spectrum as a function of depth (16,38).

The $(\overline{\mu}_{en}/\rho)^m_{LiF}$ is significantly more dependent on the medium composition than $\Psi^m_{LiF}$, as can be seen in Table 4, with values ranging from 0.4879 to 5.3019 for adipose tissue and bone, respectively. Following the methodology previously presented, the DCF is obtained from the product of $\Psi^m_{LiF}$ and $(\overline{\mu}_{en}/\rho)^m_{LiF}$ calculated parameters, validated from the $D^{MC}_{m,m}/D^{MC}_{LiF,m}$ ratios for each evaluated TEM, as shown in Fig. 4. It is observed that the dose ratios are constant despite the photon energy spectrum hardening from 1.0 to 13.0 mm thicknesses for all evaluated TEM. Table 5 presents the mean values of the $D^{MC}_{m,m}/D^{MC}_{LiF,m}$ ratios and estimated DCF, proving that they are compatible by presenting differences within their respective uncertainties. This excellent agreement validates the estimated DCF for all TEM evaluated in this work.

Using the DCF, it becomes feasible to estimate the dose to the medium obtained from the LiF experimental values, as depicted in Fig. 5. The observed uncertainties primarily arise from the average of repeated measurements and the dose calibration coefficient, as detailed in Table 3. Exhaustive experimental measurements were carried out resulting in the quality of the presented data.

In addition to the aforementioned points, it is important to note that the ratios presented in Fig. 5 are influenced by several experimental factors, as presented in the sensitivity analysis performed in the previous work (28). This analysis demonstrated that the internal source shift has a significant impact on absorbed dose of LiF. An overdosage close to 4.5–3.5 % was observed in the first millimeters of the PDD, indicating a possible downward displacement of the source in the seed, likely to gravity. This displacement would result in a closer proximity between the source and the LiF, considering the arrangement of the seed and LiF within the top and bottom slabs of the phantom, respectively, as illustrated in Fig. 1.

The main studies in the literature calculate the DCF for different media and types of beams (15–17,25). Landry et al. (16), presents DCF calculated for some human tissues to water, and vice versa, for four types of low energy BT sources. The differences in DCF due to the composition of different tissues are presented, showing variations up to 30% just by changing the ratio between adipose tissue/mammary gland in breast studies. Tedgren et al. (17) emphasize that the DCF between the medium and water is substantially more pronounced for low-energy photons compared to those widely used in BT megavoltage photons. For an energy of 20 keV, DCF values of 1.693 for adipose tissue and 0.155 for bone are presented. However, for higher-energy photons, such as those from $^{192}$Ir, the values are not as relevant, with DCF of 1.002 for adipose tissue and 1.014 for bone, stressing the importance of properly considering the medium for low energies photons.

The study by Branco et al. (25) presents the conversion factors of dose to medium for both water and LiF, showing values between 0.992 for water/bone and 0.995 for LiF/bone, considering an NS60 X-ray (ISO-4037N) (39) source with an average energy of 47.3 keV. As this source has a mean energy greater than the one for $^{125}$I, its dependence on medium composition for both water and LiF is lower.

However, the DCF presented in these studies relies solely on MC calculations. The present work, on the other hand, presents the experimental values which support the dose conversion methodology and the DCF attained values. Saguri et al. (40) present a practical methodology to quantify the dose in the bone and in the lung, similarly to the one presented in this work, using 0.089 cm thick LiF:Mg,Ti (TLD-100) dosimeter and both 6 MV and 15 MV photon beams. The obtained DCF values for bone and lung were, respectively, of 0.942 and 1.002 for 6 MV beam, and 0.927 and 1.005 for 15 MV beam, with 3% differences between experimental and calculated values. In this range, however, the composition and density of the medium are less relevant than those studied in this work.

## Conclusions

The introduction of MBDCA in BT is already a reality and relevant for clinical practices, despite the limited availability of experimental validation data in the literature. Albeit laborious, experimental MBDCA validation is feasible for low-energy BT sources. This work follows the TG-186 recommendations regarding the need to design and implement relevant physical phantom geometries with known materials to generate reference data. It refer-

ences the physical phantom presented in the previous work, proposing simple design modifications that allow dosimetric evaluations in heterogeneous media. The flexibility and cost-effectiveness of the phantom allow for parallel execution of repetitive experiments, which led to required accuracy in dose evaluations.

The obtained DCF were 0.4903 ± 0.0010 for adipose tissue, 5.1598 ± 0.0288 for bone, 0.6153 ± 0.0007 for breast 50/50, and 0.8604 ± 0.0010 for exhaled lung. These factors allowed the conversion of the LiF response into dose to medium with a precision within 6.92 % uncertainty ($k=1$). This level of accuracy is considered excellent for dosimetry with low-energy BT sources, given the inherent challenges of performing accurate experimental measurements in regions with high-dose gradients.

The significance of this work lies in providing a comprehensive dataset of four different tissue equivalent materials that validates the dose conversion methodology, the DCF factors attained for each of the TEM studied on this work, and supports the MBDCA-based TPS. The experimental validation of the conversion methodology is extremely important for the clinical procedures, as it can be further extended to the conversion to dose to water ($D_{w,w}$), and thus associate the dose to medium with reference values widely used in clinical practice.

## Acknowledgments

PCGA acknowledges CNEN (Comissão Nacional de Energia Nuclear) for a research fellowship.

## References

[1] Wei S, Li C, Li M, et al. Radioactive Iodine-125 in tumor therapy: advances and future directions. *Front Oncol* 2021;11:717180. doi:10.3389/fonc.2021.717180.

[2] Li J, Yu T, Zhang L, et al. An iodine-125 seed strand combined with a metal stent versus a metal stent alone for obstructive jaundice caused by pancreatic ductal adenocarcinoma. *Brachytherapy* 2021;20:446–453. doi:10.1016/j.brachy.2020.10.004.

[3] Li S, Guo J-H, Lu J, et al. I-125 irradiation stent for treatment of hepatocellular carcinoma with portal vein thrombosis: a meta-analysis. *Cancer Radiother* 2021;25:340–349. doi:10.1016/j.canrad.2020.12.003.

[4] Pagulayan C, Heng SM, Corde S. Dosimetric validation of the Theragenics AgX–100® I–125 seed for ROPES eye plaque brachytherapy. *Australas Phys Eng Sci Med* 2019;42:599–609. doi:10.1007/s13246-019-00761-6.

[5] Smile TD, Tom MC, Halima A, et al. I-125 Interstitial brachytherapy with or without androgen deprivation therapy among unfavorable - intermediate and high-risk prostate cancer. *Brachytherapy* 2022;21:85–93. doi:10.1016/j.brachy.2021.09.001.

[6] Licciardello T, Feliciane G, Mazzotti G, et al. Radiation protection and dosimetry issues for patients with prostate cancer after I-125 low-dose-rate brachytherapy permanent implant. *Brachytherapy* 2021;20:272–278. doi:10.1016/j.brachy.2020.09.003.

[7] Henry A, Pieters BR, Siebert FA, Hoskin P. UROGEC group of GEC ESTRO with endorsement by the European Association of Urology. GEC-ESTRO ACROP prostate brachytherapy guidelines. *Radiother Oncol* 2022;167:244–251. doi:10.1016/j.radonc.2021.12.047.

[8] Jiang Y, Zhen P, Dai J, Li Y, et al. Long-term safety and efficacy of CT-guided I-125 radioactive seed implantation as a salvage therapy for recurrent head and neck squamous carcinoma: a multicenter retrospective study. *Front Oncol* 2021;1:645077. doi:10.3389/fonc.2021.645077.

[9] Nuver TT, Hilgers GC, Kattevilder RAJ, Westendorp H. Local seed displacement from Day 0 to Day 30 in I-125 permanent prostate brachytherapy: a detailed, computed tomographic-based analysis. *Brachytherapy* 2022;21:208–215. doi:10.1016/j.brachy.2021.12.009.

[10] Beaulieu L, Tedgren ÅC, Carrier JF, et al. Task Group 186 on model-based dose calculation methods in brachytherapy beyond the TG-43 formalism: current status and recommendations for clinical implementation. *Med Phys* 2012;39:6208–6236. doi:10.1118/1.4747264.

[11] Nath R, Anderson LL, Luxton G, et al. Dosimetry of interstitial brachytherapy sources: recommendations of the AAPM Radiation Therapy Committee Task Group No. 43. American Association of Physicists in Medicine. *Med Phys* 1995;22:209–234. doi:10.1118/1.597458.

[12] Rivard MJ, Coursey BM, DeWerd LA, et al. Update of AAPM Task Group No. 43 Report: a revised AAPM protocol for brachytherapy dose calculations. *Med Phys* 2004;31:633–674. doi:10.1118/1.1646040.

[13] Rivard MJ, Butler WM, DeWerd LA, et al. Supplement to the 2004 update of the AAPM Task Group No. 43 Report. *Med Phys* 2007;34:2187–2205. doi:10.1118/1.2736790.

[14] Rivard MJ, Ballester F, Butler WM, et al. Supplement 2 for the 2004 update of the AAPM Task Group No. 43 Report: joint recommendations by the AAPM and GEC-ESTRO. *Med Phys* 2017;44:297–338. doi:10.1002/mp.12430.

[15] Giménez-Alventosa V, Antunes PCG, Vijande J, et al. Collision-kerma conversion between dose-to-tissue and dose-to-water by photon energy-fluence corrections in low-energy brachytherapy. *Phys Med Biol* 2017;62:146–164. doi:10.1088/1361-6560/aa4f6a.

[16] Landry G, Reniers B, Pignol JP, et al. The difference of scoring dose to water or tissues in Monte Carlo dose calculations for low energy brachytherapy photon sources. *Med Phys* 2011;38:1526–1533. doi:10.1118/1.3549760.

[17] Tedgren ÅC, Carlsson GA. Specification of absorbed dose to water using model-based dose calculation algorithms for treatment planning in brachytherapy. *Phys Med Biol* 2013;58:2561–2579. doi:10.1088/0031-9155/58/8/2561.

[18] Yang Y, Rivard MJ. Evaluation of brachytherapy lung implant dose distributions from photon-emitting sources due to tissue heterogeneities. *Med Phys.* 2011;38:5857. doi:10.1118/1.3641872.

[19] Rivard MJ, Beaulieu L, Mourtada F. Enhancements to commissioning techniques and quality assurance of brachytherapy treatment planning systems that use model-based dose calculation algorithms. *Med Phys* 2010;37:2645–2658. doi:10.1118/1.3429131.

[20] Morato S, Juste B, Peris S, et al. Brachytherapy organ dose estimation using Monte Carlo simulations of realistic patient models. *Ann Int Conf IEEE Eng Med Biol Soc* 2018;7:6149–6152. doi:10.1109/EMBC.2018.8513678.

[21] Andreo P, Burns DT, Salvat F. On the uncertainties of photon mass energy-absorption coefficients and their ratios for radiation dosimetry. *Phys Med Biol* 2012;57:2117–2136. doi:10.1088/0031-9155/57/8/2117.

[22] Ballester F, Tedgren ÅC, Granero D, et al. A generic high-dose rate 192Ir brachytherapy source for evaluation of model-based dose calculations beyond the TG-43 formalism. *Med Phys* 2015;42:3048–3062. doi:10.1118/1.4921020.

[23] Andreo P. Dose to 'water-like' media or dose to tissue in MV photons radiotherapy treatment planning: still a matter of debate. *Phys Med Biol* 2015;60:309–337. doi:10.1088/0031-9155/60/1/309.

[24] Andreo P. Dose to 'water-like' media or dose to tissue in MV photons radiotherapy treatment planning: still a matter of debate. *Phys Med Biol* 2015;60:2619 corrigendum.

[25] Branco ISL, Antunes PCG, Fonseca GP, Yoriyaz H. Monte Carlo studies on water and LiF cavity properties for dose-reporting quantities when using x-ray and brachytherapy sources. *Phys Med Biol* 2016;61:8890–8907. doi:10.1088/1361-6560/61/24/8890.

[26] Pappas EP, Zoros E, Moutsatsos A, et al. On the experimental validation of model-based dose calculation algorithms for $^{192}$Ir HDR brachytherapy treatment planning. *Phys Med Biol* 2017;62:4160–4182. doi:10.1088/1361-6560/aa6a01.

[27] Moura ES, Micka JA, Hammer CG, et al. Development of a phantom to validate high-dose-rate brachytherapy treatment planning systems with heterogeneous algorithms. *Med Phys* 2015;42:1566–1574. doi:10.1118/1.4914390.

[28] Antunes P.C.G, Siqueira P.T.D., Shorto J.M.B. and Yoriyaz H. A versatile physical phantom design and construction for I-125 dose measurements and dose-to-medium determination. Brachytherapy; 22:80-92. doi:10.1016/j.brachy.2022.10.005.

[29] CIRS Tissue Simulation & Phantom Technology. CIRS Models 062M/062MA/062MAQ Tissue-equivalent Materials Elemental Composition Data 2013.

[30] Mckeever SWS. Thermoluminescence of solids. Cambridge University Press, Cambridge, 2011. doi:10.1017/CBO9780511564994.

[31] Duragkar A, Muley A, Pawar NR, et al. Versatility of thermoluminescence materials and radiation dosimetry - a review. *Luminescence* 2019;34:656–665. doi:10.1002/bio.3644.

[32] Davis SD, Ross CK, Mobit PN, et al. The response of lif thermoluminescence dosemeters to photon beams in the energy range from 30 kV x rays to $^{60}$Co gamma rays. *Radiat Prot Dosimetry* 2003;106:33–43. doi:10.1093/oxfordjournals.rpd.a006332.

[33] Rodriguez M, Rogers DWO. Effect of improved TLD dosimetry on the determination of dose rate constants for 125I and 103Pd brachytherapy seeds. *Med Phys* 2014;41:114301 15 pp.. doi:10.1118/1.4895003.

[34] Werner C.J., Bull J.S., Solomon C.J.J., et al. MCNP6.2 Release Notes, Los Alamos National Laboratory, report LA-UR-18-20808, 2018.

[35] Kennedy RM, Davis SD, Micka JA, DeWerd LA. Experimental and Monte Carlo determination of the TG-43 dosimetric parameters for the model 9011 THINSeedTM brachytherapy source. *Med Phys* 2010;37:1681–1688. doi:10.1118/1.3360899.

[36] DeWerd LA, Lbbott GS, Meigooni AS, et al. A dosimetric uncertainty analysis for photon-emitting brachytherapy sources: Report of AAPM task group No. 138 and GEC-ESTRO. *Med Phys* 2011;38:782–801. doi:10.1118/1.3533720.

[37] ICRP 2009 Adult reference computational phantoms ICRP Publication 110 Ann. ICRP 39 2

[38] Fonseca GP, Tedgren ÅC, Reniers B, et al. Dose specification for $^{192}$Ir high dose rate brachytherapy in terms of dose-to-water-in-medium and dose-to-medium-in-medium. *Phys Med Biol* 2015;7:4565–4579. doi:10.1088/0031-9155/60/11/4565.

[39] ISO Report 4037-1. X and gamma reference radiation for calibrating dosemeters and dose rate meters and for determining their response as a function of photon energy—part 1: radiation characteristics and production methods. International Organization for Standardization Geneva, 1997. ISO.

[40] Sarigul N, Surucu M, Reft C, et al. A practical method for quantifying dose in bone and lung using TLDs when using 6 and 15 MV photon beams. *Phys Med Biol* 2020;6:05NT01. doi:10.1088/1361-6560/ab735d.